Precision Determination of the Neutral Weak Form Factor of 48Ca

(CREX Collaboration) Adhikari, D.; Albataineh, H.; Androic, D.; Aniol, K. A.; Armstrong, D. S.; Averett, T.; Ayerbe Gayoso, C.; Barcus, S. K.; Bellini, V.; Beminiwattha, R. S.; ...

Source / Izvornik: **Physical Review Letters, 2022, 129**

Journal article, Published version
Rad u časopisu, Objavljena verzija rada (izdavačev PDF)

https://doi.org/10.1103/PhysRevLett.129.042501

Permanent link / Trajna poveznica: https://urn.nsk.hr/urn:nbn:hr:217:435894

Editors' Suggestion

Precision Determination of the Neutral Weak Form Factor of ^{48}Ca

D. Adhikari,[1] H. Albataineh,[2] D. Androic,[3] K. A. Aniol,[4] D. S. Armstrong,[5] T. Averett,[5] C. Ayerbe Gayoso,[5] S. K. Barcus,[6] V. Bellini,[7] R. S. Beminiwattha,[8] J. F. Benesch,[6] H. Bhatt,[9] D. Bhatta Pathak,[8] D. Bhetuwal,[9] B. Blaikie,[10] J. Boyd,[11] Q. Campagna,[5] A. Camsonne,[6] G. D. Cates,[11] Y. Chen,[8] C. Clarke,[12] J. C. Cornejo,[13] S. Covrig Dusa,[6] M. M. Dalton,[6] P. Datta,[14] A. Deshpande,[12,15,16] D. Dutta,[9] C. Feldman,[12,17] E. Fuchey,[14] C. Gal,[15,9,11,12] D. Gaskell,[6] T. Gautam,[18] M. Gericke,[10] C. Ghosh,[19,12] I. Halilovic,[10] J.-O. Hansen,[6] O. Hassan,[10] F. Hauenstein,[6] W. Henry,[20] C. J. Horowitz,[21] C. Jantzi,[11] S. Jian,[11] S. Johnston,[19] D. C. Jones,[20,6] S. Kakkar,[10] S. Katugampola,[11] C. Keppel,[6] P. M. King,[22] D. E. King,[23,20] K. S. Kumar,[19] T. Kutz,[12] N. Lashley-Colthirst,[18] G. Leverick,[10] H. Liu,[19] N. Liyanage,[11] J. Mammei,[10] R. Mammei,[24] M. McCaughan,[6] D. McNulty,[1] D. Meekins,[6] C. Metts,[5] R. Michaels,[6] M. Mihovilovic,[25,26] M. M. Mondal,[12,15] J. Napolitano,[20] A. Narayan,[27] D. Nikolaev,[20] V. Owen,[5] C. Palatchi,[11,15] J. Pan,[10] B. Pandey,[18] S. Park,[9,12] K. D. Paschke,[11,*] M. Petrusky,[12] M. L. Pitt,[28] S. Premathilake,[11] B. Quinn,[13] R. Radloff,[22] S. Rahman,[10] M. N. H. Rashad,[11] A. Rathnayake,[11] B. T. Reed,[21] P. E. Reimer,[29] R. Richards,[12] S. Riordan,[29] Y. R. Roblin,[6] S. Seeds,[14] A. Shahinyan,[30] P. Souder,[23] M. Thiel,[31] Y. Tian,[23] G. M. Urciuoli,[32] E. W. Wertz,[5] B. Wojtsekhowski,[6] B. Yale,[5] T. Ye,[12] A. Yoon,[33] W. Xiong,[23,34] A. Zec,[11] W. Zhang,[12] J. Zhang,[12,15,34] and X. Zheng[11]

(CREX Collaboration)

[1]*Idaho State University, Pocatello, Idaho 83209, USA*
[2]*Texas A & M University—Kingsville, Kingsville, Texas 78363, USA*
[3]*University of Zagreb, Faculty of Science, Zagreb, HR 10002, Croatia*
[4]*California State University, Los Angeles, Los Angeles, California 90032, USA*
[5]*William and Mary, Williamsburg, Virginia 23185, USA*
[6]*Thomas Jefferson National Accelerator Facility, Newport News, Virginia 23606, USA*
[7]*Istituto Nazionale di Fisica Nucleare, Sezione di Catania, 95123 Catania, Italy*
[8]*Louisiana Tech University, Ruston, Louisiana 71272, USA*
[9]*Mississippi State University, Mississippi State, Mississippi 39762, USA*
[10]*University of Manitoba, Winnipeg, Manitoba R3T2N2, Canada*
[11]*University of Virginia, Charlottesville, Virginia 22904, USA*
[12]*Stony Brook, State University of New York, Stony Brook, New York 11794, USA*
[13]*Carnegie Mellon University, Pittsburgh, Pennsylvania 15213, USA*
[14]*University of Connecticut, Storrs, Connecticut 06269, USA*
[15]*Center for Frontiers in Nuclear Science, Stony Brook, New York 11794, USA*
[16]*Brookhaven National Laboratory, Upton, New York 11973, USA*
[17]*Institute for Advanced Computational Science, Stony Brook, New York 11794, USA*
[18]*Hampton University, Hampton, Virginia 23668, USA*
[19]*University of Massachusetts Amherst, Amherst, Massachusetts 01003, USA*
[20]*Temple University, Philadelphia, Pennsylvania 19122, USA*
[21]*Indiana University, Bloomington, Indiana 47405, USA*
[22]*Ohio University, Athens, Ohio 45701, USA*
[23]*Syracuse University, Syracuse, New York 13244, USA*
[24]*University of Winnipeg, Winnipeg, Manitoba R3B2E9, Canada*
[25]*Jožef Stefan Institute, SI-1000 Ljubljana, Slovenia*
[26]*Faculty of Mathematics and Physics, University of Ljubljana, SI-1000 Ljubljana, Slovenia*
[27]*Veer Kunwar Singh University, Ara, Bihar 802301, India*
[28]*Virginia Tech, Blacksburg, Virginia 24061, USA*
[29]*Physics Division, Argonne National Laboratory, Lemont, Illinois 60439, USA*
[30]*A. I. Alikhanyan National Science Laboratory (Yerevan Physics Institute), Yerevan 0036, Armenia*
[31]*Institut für Kernphysik, Johannes Gutenberg-Universität, Mainz 55122, Germany*
[32]*INFN - Sezione di Roma, I-00185 Rome, Italy*
[33]*Christopher Newport University, Newport News, Virginia 23606, USA*
[34]*Shandong University, Qingdao, Shandong 266237, China*

(Received 23 May 2022; revised 15 June 2022; accepted 16 June 2022; published 20 July 2022)

We report a precise measurement of the parity-violating (PV) asymmetry A_{PV} in the elastic scattering of longitudinally polarized electrons from ^{48}Ca. We measure $A_{\mathrm{PV}} = 2668 \pm 106(\mathrm{stat}) \pm 40(\mathrm{syst})$ parts per billion, leading to an extraction of the neutral weak form factor $F_W(q = 0.8733\ \mathrm{fm}^{-1}) = 0.1304 \pm 0.0052(\mathrm{stat}) \pm 0.0020(\mathrm{syst})$ and the charge minus the weak form factor $F_{\mathrm{ch}} - F_W = 0.0277 \pm 0.0055$. The resulting neutron skin thickness $R_n - R_p = 0.121 \pm 0.026(\mathrm{exp}) \pm 0.024(\mathrm{model})$ fm is relatively thin yet consistent with many model calculations. The combined CREX and PREX results will have implications for future energy density functional calculations and on the density dependence of the symmetry energy of nuclear matter.

DOI: 10.1103/PhysRevLett.129.042501

Parity-violating electron scattering (PVES) can locate neutrons in nuclei with minimal model dependence since the electroweak reaction is free from most strong interaction uncertainties [1–3]. PVES measurements can be optimized to extract the thickness of the neutron skin, the excess in the root mean-square size of the distribution of neutrons over that of the protons, which depends on the pressure of neutron-rich matter as neutrons are pushed out against surface tension [4]. Recently, PREX-2 accurately measured the thickness of the neutron skin in ^{208}Pb using this technique [5].

Chiral effective field theory can predict neutron skin thicknesses using two- and three-nucleon interactions [6]. These interactions are typically measured in few-nucleon systems where important three-neutron forces [7] are difficult to probe. Although such calculations using coupled cluster wave functions for both ^{48}Ca and ^{208}Pb have now been performed [6,8], microscopic calculations are more feasible in the lighter ^{48}Ca system than for ^{208}Pb. Here, we report on a PVES measurement to constrain the neutron radius of ^{48}Ca. While the ^{208}Pb nucleus more closely approximates uniform nuclear matter, the ^{48}Ca nucleus lies in a different regime of smaller nuclei for which the neutron skin is more closely related to the details of the nuclear force. Not only is the new measurement complementary to the earlier ^{208}Pb result in this way, but it will allow direct comparison to more microscopic calculations.

More accurate neutron skin predictions across the periodic table [9–11] will be facilitated by these measurements in ^{48}Ca and ^{208}Pb. Since atomic parity violation experiments depend on the overlap of atomic electrons with neutrons, PVES neutron radii constraints along with nuclear theory may allow more precise low energy tests of the standard model [12–15]. Coherent neutrino-nucleus elastic scattering depends on neutron radii and the same weak form factor as does PVES [16,17]. PVES weak form factor measurements along with theory may improve sensitivity to nonstandard neutrino interactions. A neutron star is 18 orders of magnitude larger than a heavy nucleus yet they have similar density, and both systems are governed by the same strong interactions and equation of state relating pressure to density. [3,18–21]. Therefore, laboratory neutron skin measurements have important implications for neutron star properties, such as radius and tidal deformability [22], and are complementary to direct x-ray [23] and gravitational wave observations [24–30].

Information on the ^{48}Ca weak charge distribution is obtained by measuring the PVES asymmetry (A_{PV}) of longitudinally polarized electrons off an isotopically enriched ^{48}Ca target in Hall A at Thomas Jefferson National Accelerator Facility (JLab). At first Born approximation, A_{PV} for a spin-zero nucleus is proportional to the ratio of weak (F_W) to charge (F_{ch}) form factors as [2]

$$A_{\mathrm{PV}} = \frac{\sigma_R - \sigma_L}{\sigma_R + \sigma_L} \approx \frac{G_F Q^2}{4\pi\alpha\sqrt{2}} \frac{|Q_W| F_W(q)}{Z F_{\mathrm{ch}}(q)}, \qquad (1)$$

where σ_R (σ_L) is the elastic differential cross-section of right (left) handed electrons off the target with a four-momentum transfer squared Q^2, $q = \sqrt{Q^2}$. G_F is the Fermi constant, α is the fine structure constant, and the weak charge of ^{48}Ca is $Q_W = -26.0 \pm 0.1$ [31]. F_{ch} from existing measurements [31,59] is used to extract F_W from the measured A_{PV}. The requirements for the practical application of this formula including precise Coulomb distortion calculations [60] are described elsewhere [2].

With the PREX-2 apparatus [5] reoptimized to measure scattering from the calcium target, A_{PV} was measured at a four-momentum transfer just below the first diffractive cross-section minimum of ^{48}Ca to achieve high sensitivity to the neutron skin. Using two dipole magnets, 4°–6° scattered electrons from a 2.18 GeV beam impinging on the calcium target were directed through precisely machined collimators into the acceptance of the two High Resolution Spectrometers (HRSs) [61] placed symmetrically on either side of the beam axis. The elastically scattered electrons were focused into a peak with a momentum dispersion of about 16 m and intercepted by a single Cherenkov detector in each HRS arm consisting of a $16 \times 3.5 \times 0.5$ cm^3 fused-silica tile. Total internal reflection provided efficient Cherenkov light transmission to a photomultiplier tube (PMT) coupled to the tile. The edge of the tile was positioned to ensure a momentum cutoff at

~2 MeV below the elastic peak, thus, minimizing contributions from inelastic scattering.

The polarized electron beam was generated using circularly polarized laser light incident on a photocathode [62]. The beam polarization sign follows the handedness of the laser circular polarization selected at 120 Hz using a Pockels cell, creating 8.13 ms time windows of constant beam helicity arranged in quartet patterns ($+--+$ or $-++-$) to ensure cancellation of 60 Hz ac power pickup. The sign of each quartet was selected pseudorandomly and reported to the data acquisition system (DAQ) with a delay to suppress electronic pickup.

Production data totaling 412 Coulombs were acquired with a 150 μA beam rastered over a 4 mm^2 area on enriched ^{48}Ca targets mounted on a cryogenically cooled copper ladder. Two 1 g/cm^2 targets, with atomic ^{48}Ca percent of $95.99 \pm 0.02\%$ and $91.70 \pm 0.01\%$ were used to acquire 7.8% and 92.2% of the total data, respectively.

The PMT anode current from the ≈28 MHz scattered flux in each detector was integrated and digitized over each helicity window by high-precision 18-bit sampling analog-to-digital convertors (ADCs). The PMT was bench tested before and after the run using light sources mimicking the integrated Cherenkov light response to determine linearity under operating conditions. Linearity was cross-checked throughout the run by monitoring detector output variation with beam current. The independent asymmetry measurements from each HRS were combined with equal weight; the final data set comprised 87 M window quartets.

The beam intensity, energy, and trajectory at the target were measured with beam monitors using the same integrating data acquisition system. Three radio frequency (rf) cavities measured the beam intensity, while six rf antenna monitors (BPMs) measured beam position along the beam line, including at dispersive locations with energy sensitivity. The polarized source was tuned to minimize the average helicity-correlated changes in beam parameters on target [63]. Two techniques were used to reverse the beam polarization relative to the voltage applied to the Pockels cell. A half-wave plate (HWP) was inserted in the laser beam path, separating the data sets into alternating reversal states with a period of about ten hours. Additionally, the full production data set was divided into three parts characterized by a change in spin precession in the low energy injector which reversed (or not) the polarization sign on target relative to that at the polarized source. Averaging over these reversals further suppressed spurious helicity-correlated asymmetries in A_{PV}.

The helicity-correlated integrated beam charge asymmetry was controlled using active feedback, and averaged to −89 ppb over the run. Modulations of air-core magnets and an accelerating rf cavity placed upstream of all BPMs were used to calibrate detector sensitivities. This calibration was crosschecked with a regression analysis based on intrinsic beam fluctuations. The individual quartet measurements of A_{PV} were corrected for beam intensity, trajectory, and energy fluctuations; the helicity-correlated correction averaged to 53 ± 5 ppb over the run. Consistency checks demonstrated that the residual detector asymmetry fluctuations were dominated by counting statistics.

Two polarimeters measured the longitudinal beam polarization P_b upstream of the target. Operating continuously through the run, the Compton polarimeter used a calorimeter to measure the energy of photons scattered by the electron beam traversing an optical cavity of circularly polarized green laser light [64]. Calibration uncertainties were minimized by integrating the calorimeter response for each helicity window, thereby eliminating a low-energy threshold. Another polarimeter that detected Møller-scattered electrons from a polarized iron foil target in a 4 T magnetic field was deployed nine times periodically during the run. The results were consistent between polarimeters and combined to yield $P_b = 87.10 \pm 0.39\%$.

Calibration data were collected at reduced beam current (100 nA to 1 μA) to enable counting and tracking of individual electrons. With Cherenkov detector PMT gains increased to detect individual particle pulses in coincidence with drift chamber tracks and trigger scintillators hits, the reconstructed scattering angle and momentum were calibrated using scattered electrons from a thin carbon target and a steel-walled water flow target, mounted on a separate, water-cooled target ladder. The momentum recoil difference between elastic scattering from hydrogen and oxygen in the water target calibrates the central angle to 0.02° absolute accuracy.

Similar counting data collected with the production ^{48}Ca target were used to estimate the fractional contribution from the first three low-lying excited states in ^{48}Ca, which totaled 1.4% of the accepted rate. Calculation of the excited state asymmetries and conservative uncertainties [31] lead to the A_{PV} corrections listed in Table I. The ^{48}Ca parity-conserving transverse single-spin asymmetry A_T was independently measured [65] and, along with counting data, used to estimate a 13 ppb uncertainty in the A_T correction to A_{PV}, due to potential residual transverse beam polarization coupled to imperfect symmetry in the left-right and top-bottom acceptance.

Using a theoretically computed $A_{\mathrm{PV}}(^{40}\mathrm{Ca}) = 2430 \pm 30$ ppb [31], the A_{PV} contribution from the assayed 7.95% ^{40}Ca target fraction was calculated to be 19 ± 3 ppb. Figure 1 shows A_{PV} measurements after all corrections in roughly uniform periods, with the global average $A_{\mathrm{PV}} = 2668 \pm 106$ ppb.

To compare this result to a theoretical model, the acceptance function $\epsilon(\theta)$ provides the distribution of scattering angles intercepting the Cherenkov detectors

$$\langle A \rangle = \frac{\int d\theta \, \sin\theta \, \mathrm{A}(\theta) \frac{d\sigma}{d\Omega} \epsilon(\theta)}{\int d\theta \, \sin\theta \frac{d\sigma}{d\Omega} \epsilon(\theta)}, \tag{2}$$

TABLE I. A_{PV} corrections and corresponding systematic uncertainties, normalized to account for polarization and background fractions.

Correction	Absolute (ppb)	Relative (%)
Beam polarization	382 ± 13	14.3 ± 0.5
Beam trajectory and energy	68 ± 7	2.5 ± 0.3
Beam charge asymmetry	112 ± 1	4.2 ± 0.0
Isotopic purity	19 ± 3	0.7 ± 0.1
3.831 MeV (2^+) inelastic	-35 ± 19	-1.3 ± 0.7
4.507 MeV (3^-) inelastic	0 ± 10	0 ± 0.4
5.370 MeV (3^-) inelastic	-2 ± 4	-0.1 ± 0.1
Transverse asymmetry	0 ± 13	0 ± 0.5
Detector nonlinearity	0 ± 7	0 ± 0.3
Acceptance	0 ± 24	0 ± 0.9
Radiative corrections (Q_W)	0 ± 10	0 ± 0.4
Total systematic uncertainty	40 ppb	1.5%
Statistical uncertainty	106 ppb	4.0%

where $(d\sigma/d\Omega)$ is the differential cross section and $A(\theta)$ is the modeled parity violating asymmetry as a function of scattering angle [31]. Simulation modeling of the calibration data was used to calculate $\epsilon(\theta)$. Radiative and rescattering effects in the target change the average accepted angle by 1.5%. The mean kinematics were found to be $\langle\theta\rangle = 4.51° \pm 0.02°$ and $\langle Q^2\rangle = 0.0297 \pm 0.0002$ $(\mathrm{GeV/c})^2$. Alternative acceptance functions, calculated using geometric and magnetic tolerances but still constrained to match spectra from calibration runs, were used to calculate an uncertainty of ± 24 ppb on A_{PV} due to possible variation of $\epsilon(\theta)$.

Table I lists all significant corrections and corresponding uncertainties; the total systematic uncertainty is 40 ppb.

The weak form factor is directly related to A_{PV} in Eq (1), and is the Fourier transform of the weak charge density ρ_W,

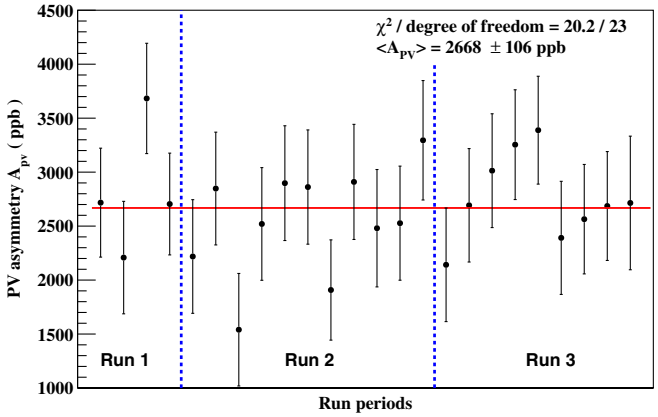

FIG. 1. Measurements of A_{PV} with statistical uncertainty; each ≈40 hour period includes two states with complementary HWP settings. The three run periods demarcate injector spin orientation reversals.

$$F_W(q) = \frac{1}{Q_W} \int d^3r\, j_0(qr) \rho_W(r). \tag{3}$$

We assume a shape for $\rho_W(r)$ and calculate A_{PV}, including Coulomb distortions and integrating over the acceptance $\epsilon(\theta)$. After adjusting the radius parameter in the $\rho_W(r)$ model [31] to reproduce the measured A_{PV}, we evaluate $F_W(q)$ in Eq. (3) using this $\rho_W(r)$ at the reference momentum transfer $q = 0.8733$ fm^{-1}. This procedure is insensitive to the form of the model ρ_W and yields the results in Table II.

While the extracted value of F_W depends on F_{ch}, F_W/F_{ch} and $F_{\mathrm{ch}} - F_W$ are quite insensitive to F_{ch}. In order to determine $F_{\mathrm{ch}}(q) = \int d^3r\, j_0(qr)\rho_{\mathrm{ch}}(r)/Z$, we use a composite charge density for ^{48}Ca starting with an accurate sum-of-Gaussians density for ^{40}Ca [66] and add a Fourier Bessel expansion for the small difference between the charge densities of ^{48}Ca and ^{40}Ca [59,67], see Ref. [31]. This procedure yields a ^{48}Ca charge radius of 3.481 fm, close to the experimental value of 3.477 fm [68].

A main result of this Letter is a measurement of the difference between charge and weak form factors,

$$F_{\mathrm{ch}}(q) - F_W(q) = 0.0277 \pm 0.0055(\mathrm{exp}). \tag{4}$$

The uncertainty is the quadrature sum of the experimental statistical and systematic uncertainties, referred to, henceforth, as the experimental error (exp), dominated by counting statistics. We emphasize that the Eq. (4) result is model independent and quite insensitive to the assumed shape for the weak density $\rho_W(r)$.

Figure 2 displays Eq. (4) for ^{48}Ca along with the PREX-2 result $F_{\mathrm{ch}} - F_W = 0.041 \pm 0.013$ for ^{208}Pb at a smaller momentum transfer of 0.3977 fm^{-1} [5]. The figure also shows a series of relativistic energy functional models with density-dependent symmetry energy slope parameter L [69,70] that varies over a large range from small negative values at the lower left to large positive values at the upper right. Additionally, a diverse collection of nonrelativistic density functional models are shown [31]. Here, F_{ch} and F_W include proton and neutron densities folded with single nucleon electric and magnetic form factors and spin orbit currents [71]. The models that best reproduce both the

TABLE II. CREX form factor results for ^{48}Ca, with q and F_{ch} input values. The uncertainties are due to statistics and experimental systematics, respectively.

Quantity	Value ± (stat) ± (sys)
q	0.8733 fm^{-1}
$F_W(q)/F_{\mathrm{ch}}(q)$	$0.8248 \pm 0.0328 \pm 0.0124$
$F_{\mathrm{ch}}(q)$	0.1581
$F_W(q)$	$0.1304 \pm 0.0052 \pm 0.0020$
$F_{\mathrm{ch}}(q) - F_W(q)$	$0.0277 \pm 0.0052 \pm 0.0020$

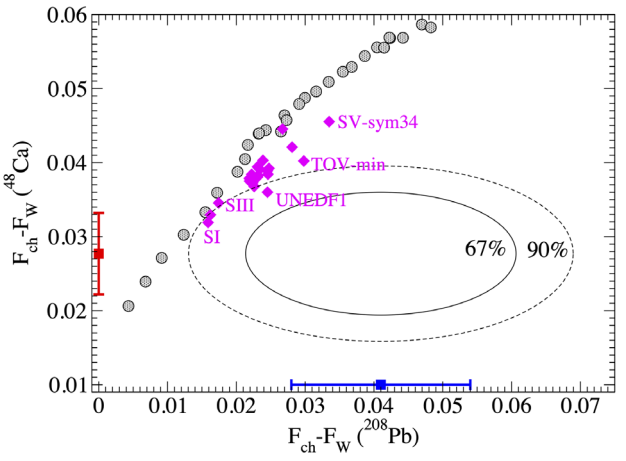

FIG. 2. Difference between the charge and weak form factors of ^{48}Ca (CREX) versus that of ^{208}Pb (PREX-2) at their respective momentum transfers. The blue (red) data point shows the PREX-2 (CREX) measurements. The ellipses are joint PREX-2 and CREX 67% and 90% probability contours. The gray circles (magenta diamonds) are a range of relativistic (nonrelativistic) density functionals. For clarity, only some of these functionals are labeled (SI [39], SIII [51], SV-sym34 [54], TOV-min [55], and UNEDF1 [57]) The complete list is in Ref. [31].

CREX and PREX-2 results tend to predict $F_{\rm ch} - F_W$ slightly below the PREX-2 result for ^{208}Pb and slightly above the CREX result for ^{48}Ca.

Figure 3 shows the momentum transfer dependence of $F_{\rm ch} - F_W$ as predicted by a few nonrelativistic and relativistic density functional models. It is evident that some model results cross as a function of q, emphasizing the somewhat different q dependence. In the limit $q \to 0$, $F_{\rm ch}(q) - F_W(q) \approx q^2(R_W^2 - R_{\rm ch}^2)/6$, where R_W is the rms

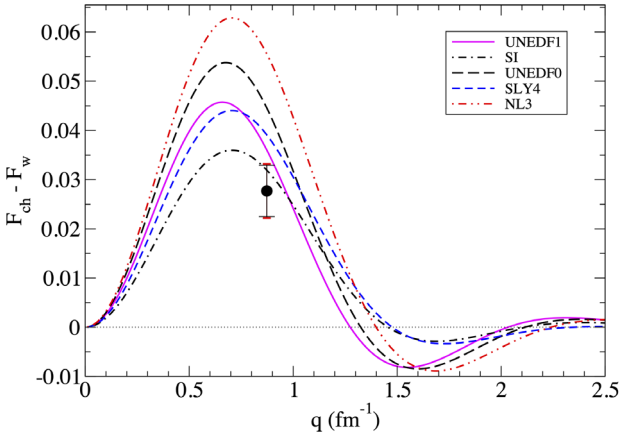

FIG. 3. The difference between the charge and weak form factors for ^{48}Ca as a function of momentum transfer $q = \sqrt{Q^2}$. The curves show results for nonrelativistic (SI, SLY4, UNEDF0, UNEDF1) and relativistic (NL3) density functional models. The CREX measurement is indicated by a circle with the inner black error bar showing the contribution from statistics and the total experimental error bar in red.

TABLE III. Extracted $R_W - R_{\rm ch}$ and $R_n - R_p$ radii. The first uncertainty is experimental and the second reflects the shape uncertainty in $\rho_W(r)$ estimated from the spread in Fig. 4.

Quantity	Value $\pm$ (exp) $\pm$ (model) (fm)
$R_W - R_{\rm ch}$	$0.159 \pm 0.026 \pm 0.023$
$R_n - R_p$	$0.121 \pm 0.026 \pm 0.024$

radius of $\rho_W(r)$ and $R_{\rm ch}$ is the charge radius. Since this equation is not valid at the larger q of CREX, the extraction of $R_W - R_{\rm ch}$ introduces some model dependence.

Relativistic and nonrelativistic density functional model predictions of $R_W - R_{\rm ch}$ versus $F_{\rm ch}(q) - F_W(q)$ are plotted in Fig. 4(a). The somewhat different $\rho_W(r)$ shapes lead to the vertical spread in the nonrelativistic models. Figure 4(b) shows a similar plot of point neutron minus proton radii $R_n - R_p$ versus $F_{\rm ch}(q) - F_W(q)$. To calculate $R_n - R_p$ given $F_{\rm ch} - F_W$, one must include full current operators including spin orbit $(\vec{L} \cdot \vec{S})$ contributions [67]. Relativistic models tend to have somewhat larger $\vec{L} \cdot \vec{S}$ currents. As a result, the gray circles in Fig. 4(b) are somewhat lower than those in Fig. 4(a) when compared to nonrelativistic models. Lines with slope matching that of the relativistic model variation are drawn to enclose the full range of displayed models, providing the model range and central values listed in Table III. This underscores the fact that the CREX ^{48}Ca $R_n - R_p$ has significant modeling uncertainty, in contrast to the PREX ^{208}Pb $R_n - R_p$, see Ref. [31]. Reduced model uncertainty would result if theoretical predictions were compared to the model-independent $F_{\rm ch} - F_W$ in Fig. 2 rather than to $R_n - R_p$ in Fig. 5.

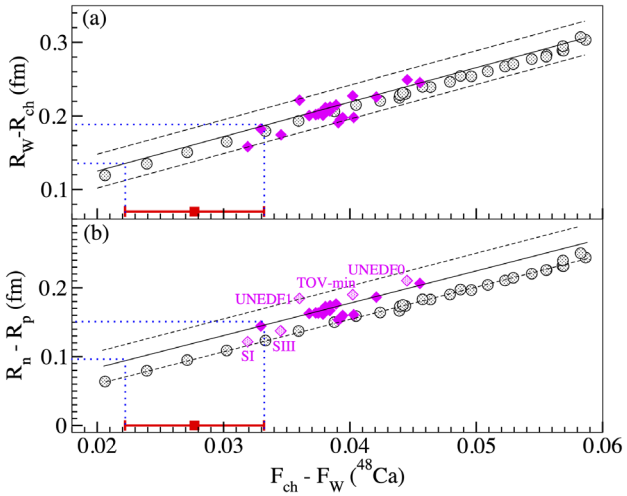

FIG. 4. (a) ^{48}Ca weak minus charge rms radius versus charge minus weak form factor at the CREX momentum transfer. The CREX experimental value and uncertainty is shown (red square). The gray circles (magenta diamonds) show a range of relativistic (nonrelativistic) density functionals. (b) ^{48}Ca neutron minus proton rms radius versus charge minus weak form factor.

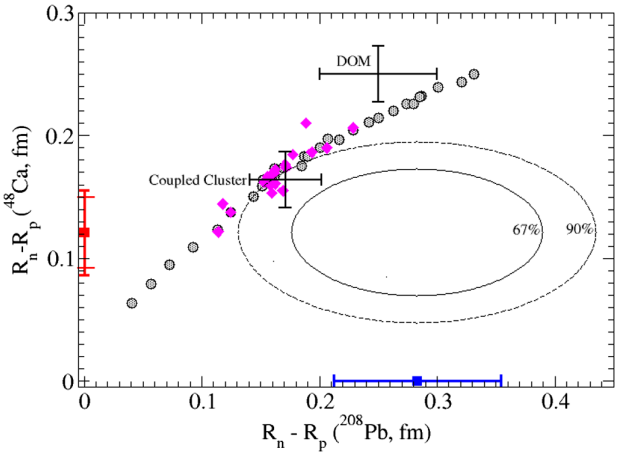

FIG. 5. ^{48}Ca neutron minus proton radius versus that for ^{208}Pb. The PREX-2 + PREX-1 experimental result is shown as a blue square, while that for CREX is shown as a red square with the inner error bars indicating the experimental error and the outer error bars including the model error. The gray circles (magenta diamonds) show a variety of relativistic (nonrelativistic) density functionals. Coupled cluster [8] and dispersive optical model (DOM) predictions [72] are also shown.

$R_n - R_p$ for ^{48}Ca versus $R_n - R_p$ for ^{208}Pb is shown in Fig. 5. A number of models including the microscopic coupled cluster calculations [8] are consistent with our results, slightly underpredicting ^{208}Pb while slightly overpredicting ^{48}Ca. Dispersive optical model calculations agree well for ^{208}Pb but substantially overpredict $R_n - R_p$ for ^{48}Ca [72].

In conclusion, we have reported a new and precise measurement of the PVES asymmetry from ^{48}Ca and a model-independent extraction of the difference between the charge form factor and the weak form factor $F_{\rm ch} - F_W$ at $q = 0.8733$ fm^{-1}. In addition, we have extracted, with a small model dependence, the weak skin $R_W - R_{\rm ch}$ and the neutron skin $R_n - R_p$ of ^{48}Ca and compared it to that of ^{208}Pb. The extracted neutron skin of ^{48}Ca (CREX) is relatively thin compared to the prediction of most models, while that of ^{208}Pb (PREX) is thick, yet both are consistent with a number of density functional models and with the microscopic coupled cluster models [8]. This will have implications for future energy density functional calculations and the density dependence of the symmetry energy.

The small model dependence of this result could be further constrained with a future measurement of $A_{\rm PV}$ from ^{48}Ca at an additional Q^2 [73]. Experimental techniques from this Letter, including excellent systematic control of helicity-correlated fluctuations and demonstration of high precision electron beam polarimetry, will inform the design of future projects MOLLER [74] and SoLID [75] at JLab measuring fundamental electroweak couplings, as well as P2 and the ^{208}Pb radius experimental proposals at Mainz [76].

We thank the entire staff of JLab for their efforts to develop and maintain the polarized beam and the experimental apparatus and acknowledge the support of the U.S. Department of Energy, the National Science Foundation, and NSERC (Canada). We thank J. Piekarewicz, P. G. Reinhard, and X. Roca-Maza for RPA calculations of ^{48}Ca excited states and J. Erler and M. Gorchtein for calculations of $\gamma - Z$ radiative corrections. This material is based upon the work supported by the U.S. Department of Energy, Office of Science, Office of Nuclear Physics Contract No. DE-AC05-06OR23177.

*paschke@virginia.edu

[1] T. Donnelly, J. Dubach, and I. Sick, Isospin dependences in parity-violating electron scattering, Nucl. Phys. **A503**, 589 (1989).
[2] C. J. Horowitz, S. J. Pollock, P. A. Souder, and R. Michaels, Parity violating measurements of neutron densities, Phys. Rev. C **63**, 025501 (2001).
[3] M. Thiel, C. Sfienti, J. Piekarewicz, C. J. Horowitz, and M. Vanderhaeghen, Neutron skins of atomic nuclei: Per aspera ad astra, J. Phys. G **46**, 093003 (2019).
[4] B. Brown, Neutron Radii in Nuclei and the Neutron Equation of State, Phys. Rev. Lett. **85**, 5296 (2000).
[5] D. Adhikari *et al.* (PREX Collaboration), Accurate Determination of the Neutron Skin Thickness of ^{208}Pb Through Parity-Violation in Electron Scattering, Phys. Rev. Lett. **126**, 172502 (2021).
[6] G. Hagen *et al.*, Neutron and weak-charge distributions of the ^{48}Ca nucleus, Nat. Phys. **12**, 186 (2016).
[7] W. Bentz and I. C. Cloët, Slope parameter of the symmetry energy and the structure of three-particle interactions in nuclear matter, Phys. Rev. C **105**, 014320 (2022).
[8] B. Hu *et al.*, *Ab initio* predictions link the neutron skin of ^{208}Pb to nuclear forces, arXiv:2112.01125.
[9] S. J. Novario, D. Lonardoni, S. Gandolfi, and G. Hagen, Trends of neutron skins and radii of mirror nuclei from first principles, arXiv:2111.12775.
[10] M. Kortelainen, J. Erler, W. Nazarewicz, N. Birge, Y. Gao, and E. Olsen, Neutron-skin uncertainties of Skyrme energy density functionals, Phys. Rev. C **88**, 031305(R) (2013).
[11] F. Sammarruca, Neutron skin systematics from microscopic equations of state, Phys. Rev. C **105**, 064303 (2022).
[12] C. S. Wood, S. C. Bennett, D. Cho, B. P. Masterson, J. L. Roberts, C. E. Tanner, and C. E. Wieman, Measurement of parity nonconservation and an anapole moment in cesium, Science **275**, 1759 (1997).
[13] M. A. Bouchiat and C. Bouchiat, Parity violation in atoms, Rep. Prog. Phys. **60**, 1351 (1997).
[14] M. J. Ramsey-Musolf, Low-energy parity-violation and new physics, Phys. Rev. C **60**, 015501 (1999).
[15] M. S. Safronova, D. Budker, D. DeMille, D. F. J. Kimball, A. Derevianko, and C. W. Clark, Search for new physics with atoms and molecules, Rev. Mod. Phys. **90**, 025008 (2018).
[16] D. Akimov *et al.*, Observation of coherent elastic neutrino-nucleus scattering, Science **357**, 1123 (2017).

[17] D. Akimov *et al.*, First Measurement of Coherent Elastic Neutrino-Nucleus Scattering on Argon, Phys. Rev. Lett. **126**, 012002 (2021).

[18] S. J. Novario, G. Hagen, G. R. Jansen, and T. Papenbrock, Charge radii of exotic neon and magnesium isotopes, Phys. Rev. C **102**, 051303(R) (2020).

[19] H. Shen, F. Ji, J. Hu, and K. Sumiyoshi, Effects of symmetry energy on the equation of state for simulations of core-collapse supernovae and neutron-star mergers, Astrophys. J. **891**, 148 (2020).

[20] C. Horowitz, Neutron rich matter in the laboratory and in the heavens after GW170817, Ann. Phys. (Amsterdam) **411**, 167992 (2019).

[21] J. B. Wei, J. J. Lu, G. F. Burgio, Z. H. Li, and H. J. Schulze, Are nuclear matter properties correlated to neutron star observables?, Eur. Phys. J. A **56**, 63 (2020).

[22] F. J. Fattoyev, J. Piekarewicz, and C. J. Horowitz, Neutron Skins and Neutron Stars in the Multimessenger Era, Phys. Rev. Lett. **120**, 172702 (2018).

[23] T. E. Riley *et al.*, A NICER view of PSR j0030 + 0451: Millisecond pulsar parameter estimation, Astrophys. J. **887**, L21 (2019).

[24] K. Chatziioannou, Neutron-star tidal deformability and equation-of-state constraints, Gen. Relativ. Gravit. **52**, 109 (2020).

[25] Y. Zhang, M. Liu, C.-J. Xia, Z. Li, and S. K. Biswal, Constraints on the symmetry energy and its associated parameters from nuclei to neutron stars, Phys. Rev. C **101**, 034303 (2020).

[26] H. Güven, K. Bozkurt, E. Khan, and J. Margueron, Multi-messenger and multiphysics Bayesian inference for the GW170817 binary neutron star merger, Phys. Rev. C **102**, 015805 (2020).

[27] L. Baiotti, Gravitational waves from neutron star mergers and their relation to the nuclear equation of state, Prog. Part. Nucl. Phys. **109**, 103714 (2019).

[28] J. Piekarewicz and F. J. Fattoyev, Constraints on the symmetry energy and its associated parameters from nuclei to neutron stars, Phys. Today **72**, No. 7, 30 (2019).

[29] M. Tsang, W. Lynch, P. Danielewicz, and C. Tsang, Symmetry energy constraints from GW170817 and laboratory experiments, Phys. Lett. B **795**, 533 (2019).

[30] M. Fasano, T. Abdelsalhin, A. Maselli, and V. Ferrari, Constraining the Neutron Star Equation of State Using Multiband Independent Measurements of Radii and Tidal Deformabilities, Phys. Rev. Lett. **123**, 141101 (2019).

[31] See Supplemental Material at http://link.aps.org/supplemental/10.1103/PhysRevLett.129.042501, which includes Refs. [32–58], for more information and Supplemental Material for a table of this function.

[32] B. G. Todd-Rutel and J. Piekarewicz, Neutron-Rich Nuclei and Neutron Stars: A New Accurately Calibrated Interaction for the Study of Neutron-Rich Matter, Phys. Rev. Lett. **95**, 122501 (2005).

[33] B. Dreher, J. Friedrich, K. Merle, H. Rothhaas, and G. Lührs, The determination of the nuclear ground state and transition charge density from measured electron scattering data, Nucl. Phys. **A235**, 219 (1974).

[34] I. Angeli and K. P. Marinova, Table of experimental nuclear ground state charge radii: An update, At. Data Nucl. Data Tables **99**, 69 (2013).

[35] P. A. Zyla *et al.* (Particle Data Group), 2020 review of particle physics, Prog. Theor. Exp. Phys. **2020**, 083C01 (2020).

[36] M. Gorchtein and C. J. Horowitz, Dispersion γZ-Box Correction to the Weak Charge of the Proton, Phys. Rev. Lett. **102**, 091806 (2009).

[37] Jens Erler and Misha Gorchtein (private communication).

[38] G. A. Lalazissis, J. Konig, and P. Ring, A new parametrization for the Lagrangian density of relativistic mean field theory, Phys. Rev. C **55**, 540 (1997).

[39] T. H. R. Skyrme, The effective nuclear potential, Nucl. Phys. **9**, 615 (1958).

[40] J. E. Wise, J. S. McCarthy, R. Altemus, B. E. Norum, R. R. Whitney, J. Heisenberg, J. Dawson, and O. Schwentker, Inelastic electron scattering from ^{48}Ca, Phys. Rev. C **31**, 1699 (1985).

[41] R. A. Eisenstein, D. W. Madsen, H. Theissen, L. S. Cardman, and C. K. Bockelman, Electron-scattering studies on ^{40}Ca and ^{48}Ca, Phys. Rev. **188**, 1815 (1969).

[42] A. M. Bernstein, V. R. Brown, and V. A. Madsen, Neutron and proton transition matrix elements and inelastic hadron scattering, Phys. Lett. **103B**, 255 (1981).

[43] J. R. Vanhoy, M. T. McEllistrem, S. F. Hicks, R. A. Gatenby, E. M. Baum, E. L. Johnson, G. Molnár, and S. W. Yates, Neutron and proton dynamics of ^{48}Ca levels and γ-ray decays from neutron inelastic scattering, Phys. Rev. C **45**, 1628 (1992).

[44] P. G. Reinhard and X. Roca-Maza (private communication).

[45] J. Piekarewicz (private communication).

[46] W.-C. Chen and J. Piekarewicz, Searching for isovector signatures in the neutron-rich oxygen and calcium isotopes, Phys. Lett. B **748**, 284 (2015).

[47] B. T. Reed, F. J. Fattoyev, C. J. Horowitz, and J. Piekarewicz, Implications of PREX-2 on the Equation of State of Neutron-Rich Matter, Phys. Rev. Lett. **126**, 172503 (2021).

[48] W.-C. Chen and J. Piekarewicz, Building relativistic mean field models for finite nuclei and neutron stars, Phys. Rev. C **90**, 044305 (2014).

[49] F. J. Fattoyev, C. J. Horowitz, J. Piekarewicz, and G. Shen, Relativistic effective interaction for nuclei, giant resonances, and neutron stars, Phys. Rev. C **82**, 055803 (2010).

[50] F. J. Fattoyev and J. Piekarewicz, Has a Thick Neutron Skin in ^{208}Pb Been Ruled Out?, Phys. Rev. Lett. **111**, 162501 (2013).

[51] D. Vautherin and D. M. Brink, Hartree-Fock calculations with Skyrme's interaction. I. Spherical nuclei, Phys. Rev. C **5**, 626 (1972).

[52] J. Bartel, P. Quentin, M. Brack, C. Guet, and H. B. Håkansson, Towards a better parametrisation of Skyrme-like effective forces: A critical study of the SkM force, Nucl. Phys. **A386**, 79 (1982).

[53] E. Chabanat, P. Bonche, P. Haensel, J. Meyer, and R. Schaeffer, A Skyrme parametrization from subnuclear to neutron star densities Part II. Nuclei far from stabilities, Nuc. Phys. **A635**, 231 (1998).

[54] P. Klüpfel, P. G. Reinhard, T. J. Bürvenich, and J. A. Maruhn, Variations on a theme by Skyrme: A systematic study of adjustments of model parameters, Phys. Rev. C **79**, 034310 (2009).
[55] J. Erler, C. J. Horowitz, W. Nazarewicz, M. Rafalski, and P. G. Reinhard, Energy density functional for nuclei and neutron stars, Phys. Rev. C **87**, 044320 (2013).
[56] M. Kortelainen, T. Lesinski, J. Moré, W. Nazarewicz, J. Sarich, N. Schunck, M. V. Stoitsov, and S. Wild, Nuclear energy density optimization, Phys. Rev. C **82**, 024313 (2010).
[57] M. Kortelainen, J. McDonnell, W. Nazarewicz, P.-G. Reinhard, J. Sarich, N. Schunck, M. V. Stoitsov, and S. M. Wild, Nuclear energy density optimization: Large deformations, Phys. Rev. C **85**, 024304 (2012).
[58] C. J. Horowitz and J. Piekarewicz, The neutron radii of Pb-208 and neutron stars, Phys. Rev. C **64**, 062802(R) (2001).
[59] H. J. Emrich, G. Fricke, G. Mallot, H. Miska, H. G. Sieberling, J. M. Cavedon, B. Frois, and D. Goutte, Radial distribution of nucleons in isotopes ^{48,40}Ca, Nucl. Phys. **A396**, 401C (1983).
[60] C. J. Horowitz, Parity violating elastic electron scattering and coulomb distortions, Phys. Rev. C **57**, 3430 (1998).
[61] J. Alcorn *et al.*, Basic instrumentation for Hall A at Jefferson Lab, Nucl. Instrum. Methods Phys. Res., Sect. A **522**, 294 (2004).
[62] C. K. Sinclair, P. A. Adderley, B. M. Dunham, J. C. Hansknecht, P. Hartmann, M. Poelker, J. S. Price, P. M. Rutt, W. J. Schneider, and M. Steigerwald, Development of a high average current polarized electron source with long cathode operational lifetime, Phys. Rev. ST Accel. Beams **10**, 023501 (2007).
[63] C. Palatchi and K. Paschke, RTP Pockels cell with nanometer-level position control, arXiv:2106.09546.
[64] M. Friend *et al.*, Upgraded photon calorimeter with integrating readout for Hall A Compton Polarimeter at Jefferson Lab, Nucl. Instrum. Methods Phys. Res., Sect. A **676**, 96 (2012).
[65] D. Adhikari *et al.* (PREX and CREX Collaborations), New Measurements of the Beam-Normal Single Spin Asymmetry in Elastic Electron Scattering over a Range of Spin-0 Nuclei, Phys. Rev. Lett. **128**, 142501 (2022).
[66] I. Sick, J. Bellicard, J. Cavedon, B. Frois, M. Huet, P. Leconte, P. Ho, and S. Platchkov, Charge density of 40Ca, Phys. Lett. B **88**, 245 (1979).
[67] H. de Vries, C. W. de Jager, and C. de Vries, Nuclear charge-density-distribution parameters from electron scattering, At. Data Nucl. Data Tables **36**, 495 (1987).
[68] G. Fricke and K. Heilig, Nuclear charge radii · 20-Ca calcium: Datasheet from Landolt-Börnstein—Group i elementary particles, nuclei and atoms · volume 20: "Nuclear charge radii", in *Springer Materials* (Springer-Verlag, Berlin, Heidelberg, 2004).
[69] J. W. Holt and Y. Lim, Universal correlations in the nuclear symmetry energy, slope parameter, and curvature, Phys. Lett. B **784**, 77 (2018).
[70] X. Viñas, M. Centelles, X. Roca-Maza, and M. Warda, Density dependence of the symmetry energy from neutron skin thickness in finite nuclei, Eur. Phys. J. A **50**, 27 (2014).
[71] C. J. Horowitz and J. Piekarewicz, Impact of spin-orbit currents on the electroweak skin of neutron-rich nuclei, Phys. Rev. C **86**, 045503 (2012).
[72] M. C. Atkinson, M. H. Mahzoon, M. A. Keim, B. A. Bordelon, C. D. Pruitt, R. J. Charity, and W. H. Dickhoff, Dispersive optical model analysis of ^{208}Pb generating a neutron-skin prediction beyond the mean field, Phys. Rev. C **101**, 044303 (2020).
[73] B. T. Reed, Z. Jaffe, C. J. Horowitz, and C. Sfienti, Measuring the surface thickness of the weak charge density of nuclei, Phys. Rev. C **102**, 064308 (2020).
[74] J. Benesch *et al.* (MOLLER Collaboration), The MOLLER experiment: An ultra-precise measurement of the weak mixing angle using Møller scattering, arXiv:1411.4088.
[75] P. Souder *et al.* (SoLID Collaboration), Precision measurement of parity-violation in deep inelastic scattering over a broad kinematic range, Technical Report No. JLAB-PR-09-012-pvdis, TJNAF, 2008.
[76] D. Becker *et al.*, The P2 experiment, Eur. Phys. J. A **54**, 208 (2018).